This is the peer-reviewed, final accepted version for American Mineralogist, published by the Mineralogical Society of America.
The published version is subject to change. Cite as Authors (Year) Title. American Mineralogist, in press.
DOI: https://doi.org/10.2138/am-2022-8415. http://www.minsocam.org/

Revision 3: Arsenic Clustering in Arsenian Pyrite: A Combined Photoemission and Theoretical Modelling Study

Reza Mahjoub*, Marta Krasowska, Nikki Stanford, William Skinner, and Philip Forson

Future Industry Institute, University of South Australia, Mawson Lakes SA 5095, Australia

ABSTRACT

Arsenian pyrite is known to have a positive correlation with gold in most auriferous refractory deposits, and thus understanding the chemical speciation of arsenic in localized environments in arsenian pyrite provides important basis for determining its reactivity and mobility. However, arsenic is fast-oxidizing amongst elements in the Fe-As-S system and hence it may exist in various chemical states, which renders it difficult to establish arsenic nature under pristine conditions, particularly in arsenian pyrite. Herein, arsenian pyrite samples were subjected to synchrotron soft X-ray spectroscopy beamline under ultra-high vacuum conditions and As-3d as well as S-2p spectra were collected. A comparison between the spectrum of bulk As-3d in the samples with its bulk counterpart in arsenopyrite revealed a 0.6 eV shift towards lower binding energies. This observation was similar to loellingite ($FeAs_2$) where the binding energy shift was attributed to high electron density on As of the As-As dimer. Formation of As clusters resulting in comparable binding energy shifts was also proposed from the spectroscopic studies. The experiments were complemented by a series of first principles calculations simulating four experimentally observed pyrite surface where superficial S atoms were randomly substituted by As. As such, six arsenian pyrite crystal surfaces were modelled, two of which constituted superficial As clusters replacing both S and Fe atoms. The surfaces were geometrically optimized, and surface energies were calculated along with the corresponding electronic structure providing a detailed distribution of partial charges for superficial atoms obtained from Löwdin population analysis. The calculated partial charges of atoms located at the surface arsenian pyrite indicated that while the electron density on the As atom of As-S dimers in arsenian pyrite is less negative than the As in bulk arsenopyrite, it is more negative for the As atom of As-As dimers, which were only seen in the superficial As clusters. This firmly validated the description of As presence in arsenian pyrite as local clusters inducing localized lattice strain due to increased bond distances. Our findings offer a good background for future studies into the reactive sites in arsenian pyrite and how that compares with associated minerals, arsenopyrite and pyrite.

35 Keywords: X-ray photoemission spectroscopy, density functional theory, pyrite, arsenian
36 pyrite

37 _____

38 * Corresponding author, electronic mail: reza.mahjoub@unisa.edu.au

39

This is the peer-reviewed, final accepted version for American Mineralogist, published by the Mineralogical Society of America.
The published version is subject to change. Cite as Authors (Year) Title. American Mineralogist, in press.
DOI: https://doi.org/10.2138/am-2022-8415. http://www.minsocam.org/

1. Introduction

The most abundant metal sulfide on the surface of Earth, including terrestrial and marine sediments, is pyrite (FeS_2). Pyrite space group is $Pa\bar{3}$ where two interpenetrating FCC structures form a halite structure. The corners of the cube and face centers are occupied by Fe atoms and sulfur dimers orienting along the <111> direction are located in the middle of the twelve edges as well as in the cube center. Consequently, each unit cell consists of four formula units of FeS_2 and each Fe is surrounded by six S as nearest neighbors forming a distorted octahedral and the bonding is described by d2sp3 hybridization of Fe valence orbitals whilst each S is tetrahedrally coordinated by three Fe and its dimer partner (Murphy and Strongin, 2009). Marcasite is another essential FeS_2 phase with space group *Pnnn*.

A broad range of potential applications has been attributed to pyrite. For example, it is a semiconductor with a band gap of ~0.95 eV, which is suited to photovoltaic cells and an optical absorption coefficient on the order of 105 cm^{-1} (much higher than that of materials like GaAs). Nevertheless, it has a very low open-circuit voltage, which causes the low efficiency of pyrite photoelectrochemical cells (Sun et al., 2011).

On the other hand, valuable sulfide ores often contain pyrite and it is well established that, pyrite surface reactivity is instrumental in processes that rely heavily on their physico-chemical properties for separation and value extraction (Hu Yuehua et al., 2009). However, pyrite is known to have poor cleavage and while the most observed cleavage direction of pyrite is (100), other cleavages comprising (021), (111) and (110) have also been experimentally detected (Murphy and Strongin, 2009). Such surfaces can be studied by either X-ray photoelectron spectroscopy (XPS) or ab initio simulations (von Oertzen et al., 2005).

Pyrite with As content above about 1 wt.% As is called arsenian pyrite (Stepanov et al., 2021; Wells and Mullens, 1973) and have been found to concentrate valuable metals such as gold (Arehart et al., 1993; Cook and Chryssoulis, 1990). In such mineralogical occurrence, a positive correlation between gold and arsenic, supported by sampling from different geological settings is observed (Palenik et al., 2004). Using first-principle and Monte Carlo calculations, Reich and Becker proposed (Reich and Becker, 2006; Reich et al., 2005) up to 6 wt.% arsenic substitution in pyrite beyond which exsolution occurred with formation of pyrite and arsenopyrite as separate phases. Based on experimental and natural data the study by Stepanov et al. (Stepanov et al., 2021) has proposed an alternative model that equilibrium solubility of As in pyrite is low and high-As pyrite is formed as metastable phase. Along the same line, the

limiting concentration of gold in arsenian pyrite was determined and expressed as $c_{Au} = 0.02 \times c_{As} + 4 \times 10^{-5}$ (Reich and Becker, 2006; Reich et al., 2005). A maximum Au/As ratio of ~0.02 was deduced for the upper compositional limit of Au and As such that, Au at concentration above this limit would form nanoparticulate gold, whereas solid solution of gold was predominant below this limit.

Understanding the distribution of As in the superficial layers of arsenian pyrite is of great theoretical and practical importance. Homogenous arsenian pyrite has not been found in nature, however back-scattered electron (BSD) images have shown arsenic-rich rim in pyrite from some deposits (Deditius et al., 2008; Liang et al., 2013; Sung et al., 2009). These arsenic-rich zones have varying arsenic concentrations and arsenic could either substitute for S (Simon et al., 1999) or Fe (Bunz et al., 2014; Deditius et al., 2008) in pyrite. In other studies, formation of As-clusters in pyrite have been proposed using high resolution transmission electron microprobe (HRTEM) analysis (Savage et al., 2000). In localized arsenic enriched zones, knowledge of the chemical bonding of arsenic in pyrite is very relevant because it provides useful information on the surface features of the minerals and how that relates to chemical processes such as oxidation and release of arsenic, and helps in the design and optimization of surface sensitive separation processes such as flotation.

While there are many ab initio studies on pyrite, a relatively smaller number of such investigations deal with the role of As in pyrites. Blanchard et al. (Blanchard et al., 2007b) explored the structure of bulk pyrite, the substitution of S by As, and the energetic of (001) pyrite surface. Their findings pointed towards substitution of S by AsS groups in bulk pyrite. Implementing DFT simulations, Chen et al. (Chen et al., 2013) found out that the existence of As is highly conductive to incorporating Au in pyrite bulk. Le Pape et al. (Le Pape et al., 2017) also used DFT calculations to simulate different substitution mechanisms for the presence of As in pyrite. Their calculations confirmed that substitution of S by As is more favourable than Fe. As another example, Santos et al. (Dos Santos et al., 2017) used DFT method with Hubbard correction to study the interface between pyrite and arsenopyrite, whereby the miscibility of these two phases was found not favourable attesting the observation of coarse coexisting crystals of pyrite with low As content and arsenopyrite.

In this work, we report on a combined photoemission and ab initio study of arsenian pyrite. The photoemission spectra from samples of arsenian pyrite collected by Synchrotron soft X-ray spectroscopy are juxtaposed by a series of first principles simulations of the four faces of

pyrite in the presence of As atoms on the top layers substituting superficial S. To improve the predictions of DFT calculations for some strongly correlated materials such as TMs with partly filled shells, DFT+U will be implemented where the correlation phenomenon resulting in a strong on-site Coulomb repulsion among electrons in a narrow d band, is represented by a spherically averaged Hubbard parameter U allowing for the increase in energy due to the insertion of an extra electron on a particular site together with a parameter J describing the screened exchange energy. As such, localized fully occupied d orbitals on one particular site are shifted to lower energies, whilst empty d orbitals are moved to higher energies (Rohrbach et al., 2003).

The inclusion of arsenic in pyrite may take place by different substitution mechanisms and resulting in different oxidation state. As explained in the review paper *Phase relations of arsenian pyrite and arsenopyrite*, while substitution of S by As is the most widespread one, the replacement of Fe by As has also been observed (Stepanov et al., 2021). Consequently, we further increase the number of As replacing both S and Fe atoms to create a cluster near the (100) and (021) surfaces and study its impact on the superficial atomic and electronic structure of pyrite.

2. Method

2.1 Synchrotron X-ray Photoelectron (SRXPS) Analysis

Laths (4 mm × 4mm × 6mm) were cut from an arsenian pyrite sample obtained from a Bolivian mine. Internal zoning of pyrite has been identified using scanning electron microscope (SEM) under backscattered electron (BSD) mode (Camscan CFSE CS44, Cambridge, UK; and Merlin, ZEISS, Australia). Spot analysis using energy-dispersive X-ray (EDX) at an accelerating voltage of 15 kv gave As concentrations oscillating from low As below limit of detect to high As concentration of 1.5-2.7 wt% as shown in Figure 1.

This is the peer-reviewed, final accepted version for American Mineralogist, published by the Mineralogical Society of America.
The published version is subject to change. Cite as Authors (Year) Title. American Mineralogist, in press.
DOI: https://doi.org/10.2138/am-2022-8415. http://www.minsocam.org/

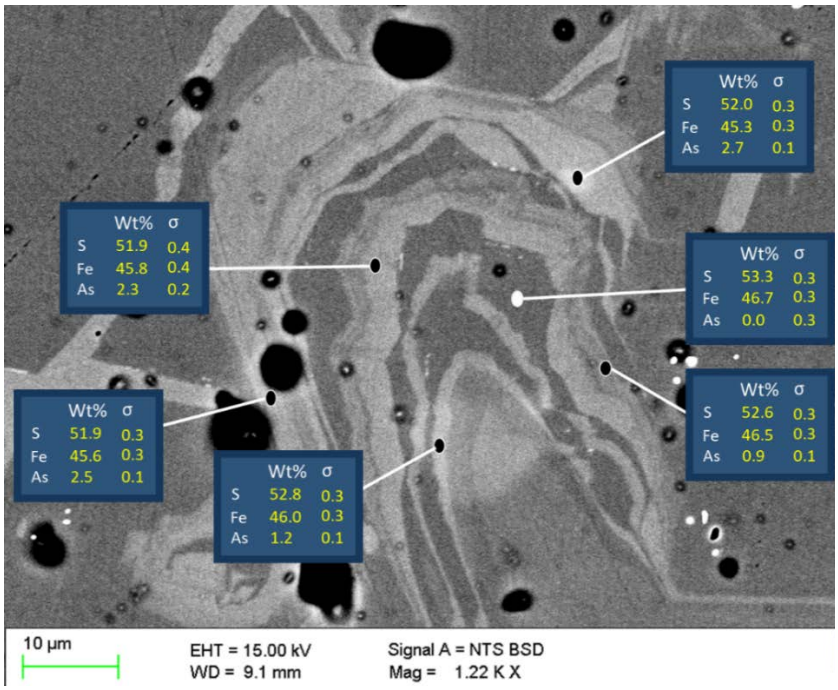

Figure 1. Back-scattered electron image of arsenian pyrite showing arsenic rich (bright) and As-poor (dark) zones in pyrite. Stoichiometry of dark spot match pure pyrite (Forson et. al. 2022, in preparation).

For comparison, pyrite and arsenopyrite samples acquired from GeoDiscoveries Australia and sourced from a Peruvian mine were prepared in the same way and analysed along with the arsenian pyrite sample. These samples where mounted onto the cleaver holder supported in place by aluminum packing pieces and a screw.

All spectra were collected at the Australian Synchrotron soft X-ray spectroscopy beamline equipped with an APPLE II UNDULATOR, 1200 line/mm monochromator grating and 20 µm monochromator exit slit. On this end station, energy resolution better than 0.2 eV is attainable at photon energies below 800 eV and resolution of about 0.2 eV at higher photon energies (~1100 eV). A SPECS Phoibos 150 electron analyser was installed with the sample positioned 80^0 to the detector. A manipulator was used to move samples from one chamber to the other.

Mounted laths were introduced into the crystal cleaver assembly, fractured under ultra-high vacuum (pressure of 1×10^{-8} Torr) and the pristine surface analysed straight away at a pressure of 2×10^{-10} Torr or better maintained throughout the analysis time. As 3d spectra were collected with a pass energy of 10 eV at photon energy of 1487 eV, 210 eV and 100 eV. S 2p spectra were collected with pass energy of 10 eV at photon energy of 1497 eV and 210 eV. Peak fitting

was carried out on CasaXPS software employing a Shirley-type background subtraction for all signals.

2.2 Calculation details

The Vienna ab initio software package (VASP) was used (Kresse and Furthmuller, 1996) implementing the projector augmented wave method to represent the combined potential of core electrons and nuclei (Kresse and Joubert, 1999). The Perdew–Burke–Ernzerhof gradient approximation was implemented to represent the exchange-correlation functional (Perdew et al., 1996). Hubbard U corrections, which are parametrized and incorporated to DFT calculations is adopted whereby Coulomb interactions are accounted for to model intra-atomic electronic correlations and the on-site Coulomb correction is represented by the difference between the Coulomb (U) and exchange terms (J) (Dudarev et al., 1998). We follow Ceder and coworkers (Sun et al., 2011) to set U=3 and J=1, which proved to provide results in good agreement with experimental measurements for bulk FeS_2 and MnS_2 (Persson et al., 2006). A cut-off energy of 400 eV was chosen for the plane wave basis and the self-consistent electronic optimization was converged to 10^{-6} eV (Mahjoub et al., 2019). A $2 \times 2 \times 1$ mesh of Γ-centered k-points was used to sample the Brillouin zone. Geometry optimization was performed using spin polarized calculations.

For (100) surface, a slab comprising $2 \times 2 \times 5$ cell was adopted with a vacuum layer of 15 $\dot{A}$ on top. The stoichiometric (2×2) cell consists of eight Fe and sixteen S atoms per surface the S-terminated slab contains eighty Fe and hundred and sixty S atoms (Zhang et al., 2012). The experimental and theoretical lattice constant of the bulk pyrite are 5.416 $\dot{A}$ (Murphy and Strongin, 2009) and 5.422 $\dot{A}$ (Zhang et al., 2012) respectively and we adopted the latter value. All other surfaces are also stoichiometric S-terminated with a 15 $\dot{A}$ vacuum on top. The dimensions of the slabs corresponding to the studied surfaces are given in Table 1. Further, superficial S atoms of all studied surfaces were randomly substituted by three As solutes. In addition, clusters of As were randomly formed on the superficial layers of (100) and (021) surfaces.

The free surface energy (σ) can be calculated as: (Alfonso, 2010; Zhang et al., 2012):

$$\sigma = (E_{FS}(N_{Fe}, N_S) - N_{Fe}\mu_{Fe} - N_S\mu_S)/2S \quad (1)$$

where E_{FS} represents the total energy of the slab-containing cell with two free surfaces and S is the surface area. μ_{Fe} and μ_S are chemical potentials with the constraint $\mu_{Fe} + 2\mu_S = \mu_{FeS_2}$ and N_{Fe} and N_S are the number of corresponding atoms in the simulation cell. The fix atoms representing bulk were located within half a lattice constant from the middle layer whilst all others were free to relax. In addition, to increase the length of the free surface layers above the fixed bulk atoms, we considered the bottom-most layer atoms fixed (Krishnamoorthy et al., 2012; von Oertzen et al., 2005) as long as their out of plane coordinates are equal or less than a lattice constant.

In the case of surface with As impurity, the aforementioned constraint on chemical potentials of Fe and S still holds and the surface energy will be expressed as

$$\sigma = (E_{FS}(N_{Fe}, N_S, N_{As}) - N_{Fe}\mu_{Fe} - N_S\mu_S - N_{As}\mu_{As})/2S \quad (2)$$

3. Results

3.1 experimental observations

All arsenic peaks where fitted with doublets, As $3d_{5/2}$ and As $3d_{3/2}$, with an energy splitting of 0.7 eV and the same FWHM (Nesbitt et al., 2002). By theory, the As $3d_{3/2}$ feature found at higher binding energy was constrained to an intensity, exactly two thirds that of the lower binding energy As $3d_{5/2}$ peak (Jones et al., 2003; Nesbitt et al., 2002).

Relative to the background, the intense peak located at 40.8 eV was assigned to bulk fully coordinated arsenic (Figure 2). The lower binding energy of the bulk As compared to common minerals in the Fe-As-S system suggests As is present at a nominal oxidation state of -1 similar to arsenopyrite and loellingite (Nesbitt et al., 2002; Schaufuss et al., 2000). In such environments, it is more likely that As will substitute for S rather than Fe (Pierre et al., 2018). This bulk As 3d spectrum of arsenian pyrite in comparison with arsenopyrite reveal a binding energy shift of about 0.6 eV, with bulk As 3d spectrum of arsenopyrite found at higher binding energy with respect to arsenian pyrite. Harmer and Nesbitt (2004) made similar observation comparing the bulk As signal of loellingite and arsenopyrite (with space groups of $P2_1/c$ and *Pnnm* respectively), where a difference of 0.5 eV existed between the two mineral phases. These authors argued that the observed difference could signify a higher electron density on As atoms of As-As dimers of loellingite compared to those of the As-S dimer of arsenopyrite.

This is the peer-reviewed, final accepted version for American Mineralogist, published by the Mineralogical Society of America.
The published version is subject to change. Cite as Authors (Year) Title. American Mineralogist, in press.
DOI: https://doi.org/10.2138/am-2022-8415. http://www.minsocam.org/

S has a higher electronegativity compared to As, thus, the decreased electron density on the As atom of As-S dimer could be the result of displaced electron density by S of As-S dimer.

Electronic structure calculations (Blanchard et al., 2007a) for arsenic substitution in pyrite showed that substitution of one As_2 unit for S_2 group in pyrite was energetically unfavorable. Assuming this assertion is valid, a second explanation is provided for the lower binding energy of the bulk As spectra of arsenian pyrite. Savage et al. (Savage et al., 2000) in a study using high resolution transmission electron microprobe (HRTEM) and X-ray absorption fine-structure spectroscopy (EXAFS) reported that As present in arsenian pyrite exists as local As clusters in lattice of pyrite. Such substitution mechanism could produce localised lattice strain from an increased chemical bond distances producing a corresponding shift in the binding energy (Richter et al., 2004). It was thus suggested that the lower binding energy of the bulk component may indicate the existence of As clusters in the arsenian pyrite sample, investigated further herein using first principle calculations.

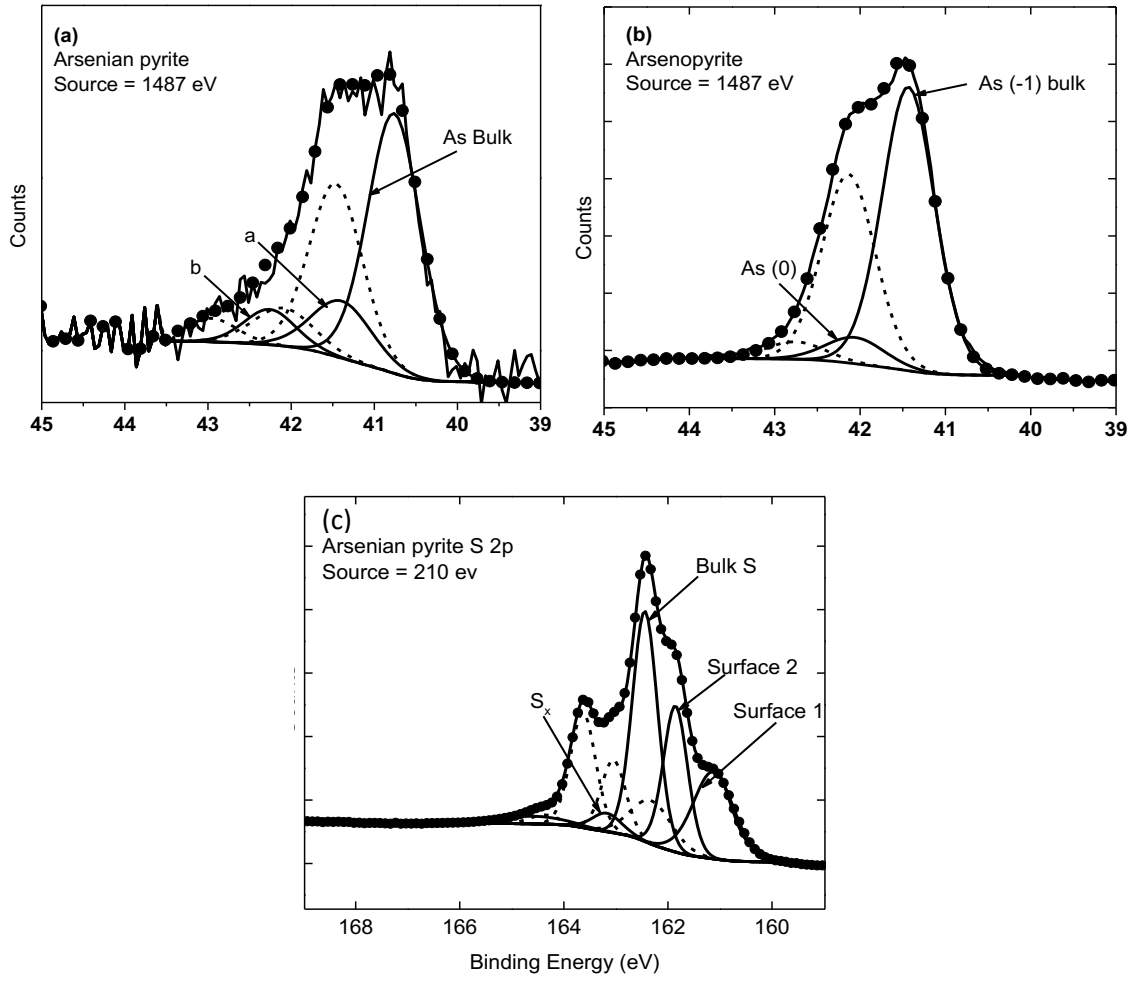

Figure 2. As 3d spectra of fractured (a) arsenian pyrite and (b) arsenopyrite at 1487 eV indicating a shift in bulk binding energies. S 2p of arsenian pyrite at 210 eV revealing contribution from various surface species is shown in (c). The doublets of the individual peaks are represented by short dashes

The S 2p spectra was fitted with doublets separated by 1.19 eV and an optimum ratio of 0.50 between the intensity of the 2p3/2 and 2p1/2 components (Figures 1a and 1b). Each doublet was constrained to have the same FWHM. To interpret the peak contributions, the S 2p of pyrite by Schaufuss, A.G. et al. (Schaufuß et al., 1998) was used. The major component at 162.4 eV was identified as the bulk signal with a slight shift in binding energy (0.1 eV) with respect to the bulk signal from pyrite (Schaufuß et al., 1998). The minor peak at 161.2 eV and 161.9 eV (Figure 2a) were in similar peak positions as pyrite with equivalent FWHMs, thus, they were assigned to surface peaks emanating from fracture of S-S and Fe-S or As-S bonds respectively. Contribution from the high binding energy component at 163.2 eV may have been from a bulk polysulphide-like species, formed from possible exsolution of sulphur at As-rich boundaries. The explanation offered is supported by the absence of oxygen, which could form components at such high binding energies.

3.2 Theoretical results

3.2.1 Surface energies

As shown in Table 1, the number of atoms, cell size, and in particular, the slab dimension normal to the surface used herein are larger than the above-reviewed references except for Zhang et al. (2012) (Zhang et al., 2012). The surface energies are listed in Table 1 for PBE+U methods which are consistent to those provided in the reference by Zhang et al. (2012) (Zhang et al., 2012). The order of stability of surfaces can thus be arranged as (100) > (111) > (110) > (021). While the substitution of superficial As atoms leads to a decrease in surface energies and hence makes them more stable as shown in Table 1, the order of stability remains the same. Difference in superficial energies could result in sector zoning, that is a major indication of surface-controlled growth as speculated by Stepanov et al. (Stepanov et al., 2021).

Were the fixed atoms representing the bulk considered at the bottom of the slab, the surface energies would be 0.993, 1.348, 1.375, 1.409 J/m^2 for (100), (111), (110), and (021) respectively. It is also noticed that the surface energies provided by DFT+U scheme are generally smaller than those by PBE.

This is the peer-reviewed, final accepted version for American Mineralogist, published by the Mineralogical Society of America.
The published version is subject to change. Cite as Authors (Year) Title. American Mineralogist, in press.
DOI: https://doi.org/10.2138/am-2022-8415. http://www.minsocam.org/

3.2.2 Electronic density of states

The superficial electronic density of states was computed using both spin-polarized and non-spin polarized calculations for the slabs wherein bottom atoms were considered fixed to represent bulk, thereby maximizing the number of surface layers free to relax. The band gap provided by DFT+U scheme for bulk agrees very well with the experimental value (0.95 eV) (Ennaoui et al., 1993). For low spin (100) surface we found a value of 0.95 eV, which is close to the findings of Sun et al. (2011) (Sun et al., 2011). For other surfaces, no band gap was detected in both low and high spin approaches. The ground state energies of the supercells representing the simulated surfaces indicated the low spin (LS) state as the favoured over the high spin (HS) state.

Figures 2(a) and (b) show the angular momentum projected density of states (pDOS) of (100) surface without and with As atoms respectively.

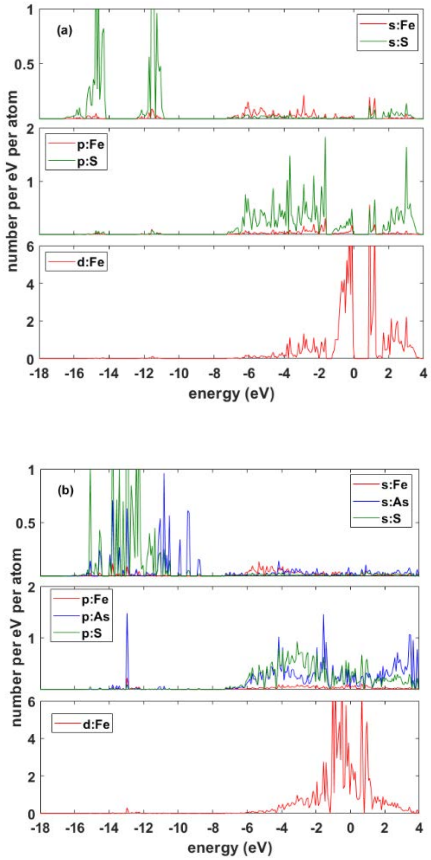

Figure 3: Local pDOS of superficial layers up to 2.7 A° from the (100) surface in (a) pyrite and (b) pyrite with a cluster of As.

It is seen that in the vicinity of the Fermi energy (E_F) DOS is dominated by the d-orbital of Fe followed by the contribution of p-orbital of S, whereas well below E_F, the DOS is governed by the s-orbital of S. The DOS peak profile also indicates strong hybridization between the p bands of S and d band Fe. The same description holds as As substitutional atoms are introduced in the superficial layers thereby increasing the number of valence electrons and shifting E_F to the lower energies (Savage et al., 2000) leading to the elimination of the narrow bandgap of the pyrite surface.

3.2.3 Charge population analysis

In the context of linear combination of atomic orbitals (LCAO) the molecular orbital can be square-integrated over all space and thus obtain the overlap population (OP). Mulliken partitioned the integration and attributed the overlap population to bonding (Dronskowski, 2005). The atom-centered electrons are customarily called atomic net population (NP). The addition of NP and OP gives the total number of electrons. Atomic gross population can be defined as the addition of NP to the symmetrically split overlap population (OP/2). As such, the atomic charge is the difference between the atomic number Z and gross population. Mulliken population analysis has been widely used in quantum chemical studies. Nevertheless, there are deficiencies in this scheme, amongst others, is the symmetrical splitting of overlap population, not least in strongly polar covalent bonds. Löwdin suggested an alternative analysis wherein symmetrical splitting of OP is substituted by the one which preserves the molecular dipole moment (Dronskowski, 2005). To provide an orthogonal basis, Löwdin implemented a symmetric transformation for all orbitals and this orthogonalization removed all overlap terms thereby avoiding overlap partition problem in Mulliken scheme. We have calculated both Mulliken and Löwdin charges, although only the latter was visualized for the atoms on and the vicinity of surfaces.

First, the computed Löwdin charges of pyrite with the space group of Pa3, arsenopyrite (FeAsS) with a monoclinic structure, and loellingite ($FeAs_2$) in the bulk state are listed in Table 2. Next, the relaxed surfaces listed in Table 1 are investigated both in pure state and with As atoms randomly substituting sulfurs on the top layers (Blanchard et al., 2007a) and the Löwdin charges of the superficial atomic layers are calculated. The charges of As and S atoms are then compared with the charges of their counterparts in bulk arsenopyrite and pyrite respectively as benchmark and the difference ($\Delta C_L = C_L^{surface} - C_L^{bulk}$) was provided in Table 3 together with schematics (Momma and Izumi, 2011) of the corresponding surface configurations. Thus, a

negative value for ΔC_L indicates a surplus electronic charge whereas a positive value implies electronic charge deficit with respect to bulk. Included in the results are the Löwdin charges of two clusters of As in the vicinity of (100) and (021) surfaces (Tables 3(c) and 3(f) respectively), which were created by substituting both S and Fe (Bunz et al., 2014) species with As. It is worth noting that while the charges are to a large extent correlated to the coordination number (CN) of the species, the values may fluctuate due to the fluctuation of bond distances caused by broken surface bonds. As such, in each atomic layer, the charge of elements with a given CN is represented by their mean value (Ertural et al., 2019).

4. Discussions

We begin by (100) surface charges (Table 3(a)) wherein the S atoms in the first atomic layer secure surplus charges of -0.10 and -0.05 for 3-folded and 4-folded CNs respectively. In the second atomic layer, while all S atoms are 4-fold coordinated, they show both deficit (+0.04) and surplus charges (-0.01). The latter S is bonded to 6-fold coordinated Fe (with a charge of 0.43) and 4-fold coordinated S much similar to the bulk, whereas the former bonds to a 5-fold coordinated Fe (with an unadjusted charge of +0.57). Indeed, we observe four values for the superficial S i.e., one is equal to the bulk S, two securing surplus charges and one enduring deficit charges comparing to the bulk. As a consequence, it is expected that in the spectra of 2p-S, two peaks shift to lower binding energies (BE) and one peak moves to higher BE, the latter corresponding to S_x in Figure 2(c).

As for the (100) surface with 3×As, atoms in the top layer are seen to have displaced to some extent in particular those located in the vicinity of the solutes. Table 3(b) indicates that compared to the bulk state of arsenopyrite or loellingite, As atoms invariably lose charge to neighbouring S and not least the 3-fold coordinated As, which loses almost 75% of its charge in bulk state ending up with a +0.12 charge deficit. While a larger range of surplus charges are calculated for S, they can be categorized in three different mean values; two of which are with surplus and one with a deficit charge with respect to the bulk.

Next, we turn attention to a cluster of 12×As atoms located near the (100) surface where local disorder seems to prevail both in atomic configuration and in charge distribution as provided in Table 3(c). While the CN of S ranges from 2 to 4, Fe may have a CN of 3 to 6. For As, the coordination varies from 2 to 4 and an ever-varying chemical environment appears where As atoms belonging to As-S dimers suffer an even worse charge deficit than their counterpart in bulk arsenopyrite. However, an exception is noticed where an As-As dimer with a bond length

of 2.4 A°, which is slightly shorter than that of loellingite (~2.55 A°) is formed in the cluster, exhibiting an opposite trend, and securing a surplus charge.

Turning attention to the topmost layer of (021), the CN of S reduces to one Fe atom, which is four-fold coordinated. As a result, S gains a surplus charge of -0.15 compared to the bulk as shown in Table 3(d). The S atoms in the next sublayer is coordinated with three Fe, the latter being six, five and four-fold coordinated respectively. Thus, the surplus charge of S increases to -0.26 compared to the bulk. Further down, while the coordination of S atoms remains three, a S-S dimer is formed and as a consequence, the surplus charge decreases to -0.06. No significant change can be seen for the charge of four-folded S atoms in the second layer. However, in the third layer, charge distribution on the three folded and four-folded S atoms is significantly different from those S in the first and second layers with the same number of nearest neighbours. This different charge distribution can be attributed to different CN's of their nearest neighbour Fe atoms, which are six-fold (for S with -0.01 surplus) and five and two six-fold coordinated (for S with +0.05 deficit charge).

The three As substituted on the (021) surface creates more disorder than on (100) and hence an S atom with two nearest neighbours appear on the top layer (one of which is bonded with a superficial As) whereby increasing the mean surplus charge to -0.20. The three-folded As in the first layer belongs to an As-S dimer and expectedly shows a deficit charge of +0.07. As anticipated, the charge distribution on the four-folded As in the second layer (including an As-S bond) undergoes a deficit of +0.18 with respect to the arsenopyrite bulk, the charge of four-folded As atom in the first layer almost stays the same. This can be associated with the small CN of the S atom (i.e., 2) and its very strong bonding with its neighbouring Fe.

Moving on to the cluster of 15×As at (021), the local configuration appears rather more chaotic than the case of As cluster on (100). Similar to the previous cluster, the As atoms bonding with a nearby S endure significant charge deficit. However, the As atom in the first layer neighbouring an atom of Fe and forming an As-As dimer with a bond length of 2.4 A°, achieves a charge surplus of -0.03 compared to the As in bulk arsenopyrite. As for S atoms, they exhibit roughly two different levels of charge surplus with respect to the S in bulk pyrite.

The distribution of charges on (110) and (111) surfaces, listed in Tables 3(g) and 3(i) respectively, are almost similar to the (100) and (021) surfaces. While the superficial S atoms near (110) surface exhibit both surplus and deficit charges species than the bulk pyrite, in the vicinity of (111) surface, the three and four-fold coordinated S atoms secure surplus charges

without deficit. The addition of As on these surfaces disrupts the chemical environment yielding both surplus and deficit charges for surface S atoms with respect to the bulk pyrite as provided in Tables 3(h) and 3(j). The As atoms form As-S dimers and while they lose charge and endure deficit with respect to bulk arsenopyrite, they do not become positively charged as for some As atoms in the cluster cases.

It is noteworthy that the nearest neighbours and coordination numbers of Tables 2 and 3 were provided considering the bonding distance of S-S, S-Fe, S-As, and Fe-As similar to those in pyrite and arsenopyrite, namely, ~2.2, 2.837, 2.846, and 2.506 A° respectively. The bond distance between two As atoms in the relaxed structure of cluster-containing surfaces found to be ~2.4 A° which is very close to that in loellingite i.e., 2.49 A° (the distance to the next nearest As neighbours is 2.88 and 3.30 A° (Nesbitt et al., 2002)). Inspired by the insight and analysis of Nesbitt et al. (Nesbitt et al., 2002) on the likelihood of polymer formation between superficial As atoms of fractured surfaces of pyrite or loellingite, we assessed the distances between all pairs of As in the relaxed structure of As clusters. It was found that As forms respectively a tetramer and a trimer in the superficial clusters of (100) and (021) surfaces an the largest distance between two adjacent As atoms equal to ~2.97 A°.

Finally, while the context of the present work is thermodynamics rather than kinetics, calculating the energetic of As substitution at different sites provides a remarkable clue to the existence of an all-important driving force for the migration of As (Nesbitt et al., 1995) to more favourable superficial sites. As such, an As was substituted individually in two different sites on (100) surface and the system was relaxed as shown in Figure 5. It was found that the supercells representing a slab with an As located individually on those different surface sites have excess energies of 0.24 and 1.07 eV respectively compared to the supercell with no superficial impurity. This is consequently reflected on their calculated surface energies as 0.895 and 0.836 J/m^2 respectively.

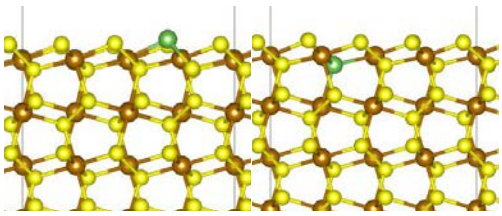

Figure 5: As substituted individually in two different sites (green) on the (100) surface.

5. Implications

The combined XPS X-ray spectroscopy and DFT study presented herein provides an understanding of possible arsenic environment in arsenian pyrite. The oxidation of pyrite and release of arsenic from sulfarsenide minerals generates environmental poisonous by-products. The enrichment of As in pyrite has been suggested to enhance its susceptibility to natural processes such as weathering (Savage et al., 2000). On the other hand, the fate of invisible gold mineralisation has often been tied to As substitution in pyrite where a positive correlation is proposed. Our findings offer a good background for future studies into the reactive sites in arsenian pyrite and how that compares with associated minerals, arsenopyrite and pyrite.

Acknowledgement

The experimental investigation was undertaken on the Soft X-ray beamline at the Australian Synchrotron, part of ANSTO. We would like to specially thank Dr Bruce Cowie for his assistance on beamtime (Proposal number 15669).

Appendix: Hubbard parameters: LDAU=TRUE, LDAUTYPE=2 (Dudarev approach), LDAUL= 2 -1 (the former refers to Fe and the latter to S), LDAUU= 3.00 0.00, and LDAUJ= 1.00 0.00.

Surface	Cell dimension ($\times$ 5.422 $\dot{A}$)	Number of Atom	Surface energy (J/m^2)	
			Pyrite	Pyrite+3As
(100)	2.×2.×7.5	240	0.826	0.840
(110)	2.828 ×2.×7.	288	1.241	1.314
(111)	2.828×2.449×6.	288	1.117	1.073
(012)	2.236 ×2.×7.232	240	1.289	1.398

Table 1: Simulation cell dimensions, number of atoms, and surface energy of the surfaces studied herein.

This is the peer-reviewed, final accepted version for American Mineralogist, published by the Mineralogical Society of America.
The published version is subject to change. Cite as Authors (Year) Title. American Mineralogist, in press.
DOI: https://doi.org/10.2138/am-2022-8415. http://www.minsocam.org/

Bulk	Fe	CN	S	CN	As	CN
Pyrite	0.44	6 (6S)	-0.22	4 (S, 3Fe)	NA	NA
Arsenopyrite	0.47	6 (3S, 3As)	-0.27	4 (As, 3Fe)	-0.20	4 (S, 3Fe)
Loellingite	0.44	6 (6As)	NA	NA	-0.22	4 (As, 3Fe)

Table 2: Löwdin charges at bulk state

surface (100)				ΔC_L		
Surface	**element**	**CN**	**NN**	**min**	**max**	**mean**
1a	S	3	S, 2Fe	-0.10	-0.10	-0.10
1c	S	4	S, 3Fe	-0.05	-0.05	-0.05
2a	S	4	S, 3Fe	0.04	0.04	0.04
2c	S	4	S, 3Fe	-0.01	-0.01	-0.01

Table 3(a): Löwdin atomic charge difference for (100) superficial layers. ΔC_L is the charge difference with respect to bulk arsenian pyrite. CN and NN are coordination number and nearest neighbours respectively.

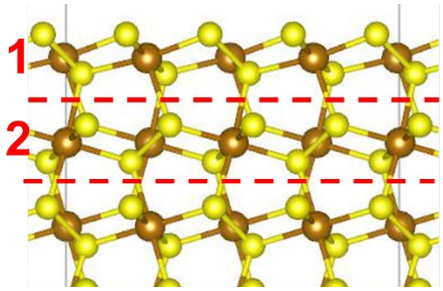

Figure 4(a): Schematic of (100) surface. Broken lines are drawn to guide eyes to atomic layers where the charges are located.

surface (100) + 3×As				ΔC_L		
Surface	**element**	**CN**	**NN**	**min**	**max**	**mean**
1a	S	3	As, 2Fe	-0.08	-0.17	-0.17
1a	As	3	S, 2Fe	0.12	0.12	0.12
1a	S	3	S, 2Fe	-0.02	-0.12	-0.09
1c	As	4	S, 3Fe	0.12	-0.01	0.06
1c	S	4	S, 3Fe	0.05	-0.09	0.00
1c	S	4	4Fe	-0.21	-0.21	-0.21
2a	S	4	S, 3Fe	0.14	0.08	0.11
2c	S	4	S, 3Fe	0.09	0.06	0.08

Table 3(b): Löwdin atomic charge difference for (100)+3×As superficial layers. For S and As, ΔC_L is the charge difference with respect to bulk arsenian pyrite and bulk arsenopyrite respectively. CN and NN are coordination number and nearest neighbours respectively.

This is the peer-reviewed, final accepted version for American Mineralogist, published by the Mineralogical Society of America.
The published version is subject to change. Cite as Authors (Year) Title. American Mineralogist, in press.
DOI: https://doi.org/10.2138/am-2022-8415. http://www.minsocam.org/

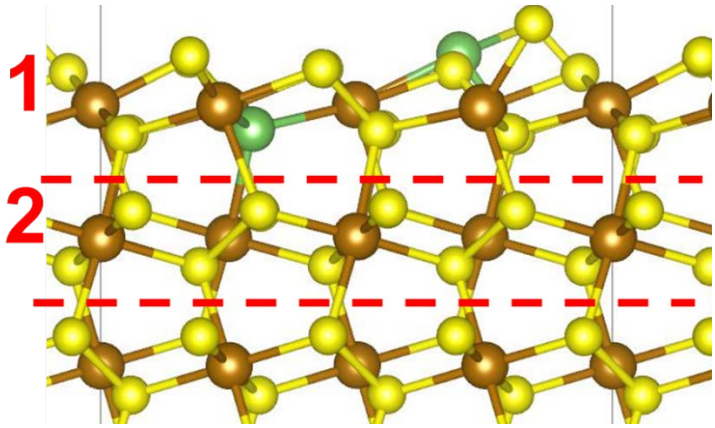

Figure 4(b): Schematic of (100) surface with three As.

surface (100)+As cluster				ΔC_L		
Surface	**element**	**CN**	**NN**	**min**	**max**	**mean**
1a	S	2	2Fe	-0.12	-0.18	-0.16
1b	S	3	S(As), 2Fe	-0.03	-0.15	-0.11
1c	As	2	2S	0.29	0.29	0.29
1d	As	2	S, Fe	0.20	0.20	0.20
2d	S	3	As, 2Fe	-0.07	-0.15	-0.11
2e	S	4	S(As), 3Fe	-0.16	-0.29	-0.21
2e	As	3	S, 2Fe	0.09	0.09	0.09
2d	As	3	3S	0.38	0.38	0.38
3a	As	3	As, 2Fe	-0.07	-0.07	-0.07
3a	As	3	S, Fe, As	0.23	0.23	0.23
3a	S	3	As, 2Fe	-0.04	-0.04	-0.04
3b	S	4	S(As), 3Fe	0.04	-0.09	-0.01
3c	As	3	3As	0.22	0.22	0.22
3c	As	3	S, 2As	0.29	0.29	0.29
3d	As	4	S, 2Fe, As	0.20	0.20	0.20
3d	S	4	S(As), 3Fe	0.03	-0.13	-0.03

Table 3(c): Löwdin atomic charge difference for (100) with As cluster. For S and As, ΔC_L is the charge difference with respect to bulk arsenian pyrite and bulk arsenopyrite respectively. CN and NN are coordination number and nearest neighbours respectively.

This is the peer-reviewed, final accepted version for American Mineralogist, published by the Mineralogical Society of America.
The published version is subject to change. Cite as Authors (Year) Title. American Mineralogist, in press.
DOI: https://doi.org/10.2138/am-2022-8415. http://www.minsocam.org/

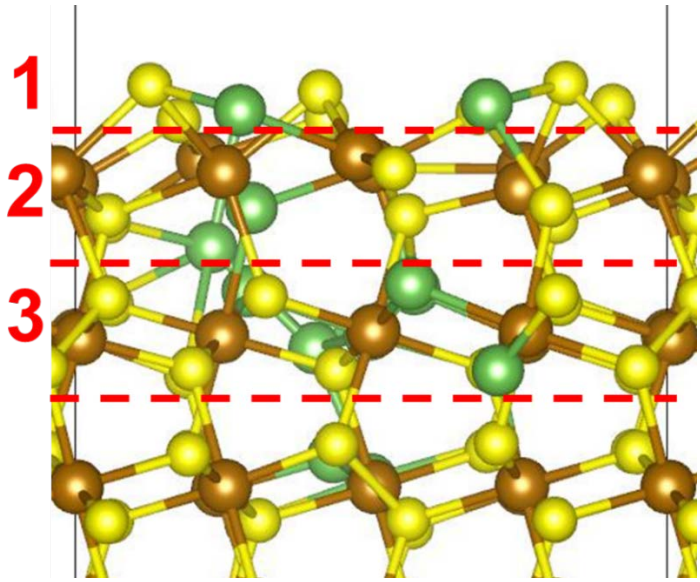

Figure 4(c): Schematic of (100) surface with an As cluster.

surface (021)				ΔC_L		
Surface	**element**	**CN**	**NN**	**min**	**max**	**mean**
1a	S	1	Fe	-0.15	-0.15	-0.15
1c	S	3	3Fe	-0.26	-0.26	-0.26
2b	S	3	S, 2Fe	-0.06	-0.06	-0.06
2c	S	4	S, 3Fe	0.01	0.01	0.01
3b	S	3	3Fe	-0.01	-0.01	-0.01
3c	S	4	S, 3Fe	0.05	0.04	0.05

Table 3(d): Löwdin atomic charge difference for (021) superficial layers. ΔC_L is the charge difference with respect to bulk arsenian pyrite. CN and NN are coordination number and nearest neighbours respectively.

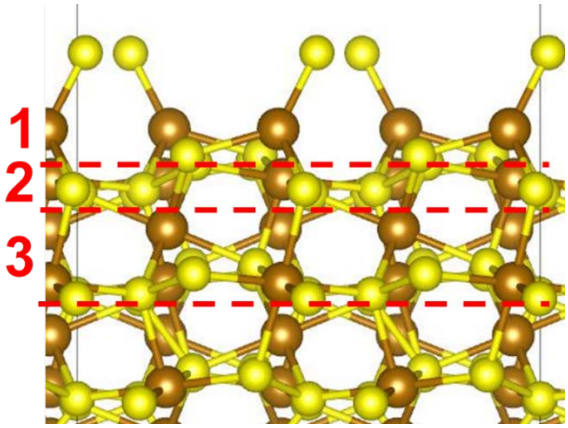

Figure 4(d): Schematic of (210) surface.

This is the peer-reviewed, final accepted version for American Mineralogist, published by the Mineralogical Society of America.
The published version is subject to change. Cite as Authors (Year) Title. American Mineralogist, in press.
DOI: https://doi.org/10.2138/am-2022-8415. http://www.minsocam.org/

surface (021)+3×As				ΔC_L		
Surface	**element**	**CN**	**NN**	**min**	**max**	**mean**
1a	S	2	S (As), Fe	-0.17	-0.24	-0.20
1	As	3	S, 2Fe	0.07	0.07	0.07
1	As	4	S, 3Fe	-0.01	-0.01	-0.01
1c	S	3	S, 2Fe	0.03	-0.11	-0.02
1d	S	4	S (As), 3Fe	-0.07	-0.09	-0.08
2b	S	4	S, 3Fe	0.07	0.03	0.06
2	As	4	S, 3Fe	0.18	0.18	0.18
3b	S	4	S, 3Fe	0.06	-0.03	0.01

Table 3(e): Löwdin atomic charge difference for (021)+3×As superficial layers. For S and As, ΔC_L is the charge difference with respect to bulk arsenian pyrite and bulk arsenopyrite respectively. CN and NN are coordination number and nearest neighbours respectively.

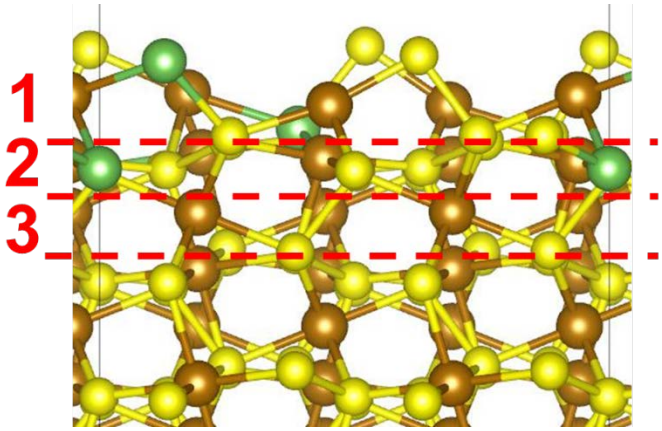

Figure 4(e): Schematic of (021) surface with three As.

This is the peer-reviewed, final accepted version for American Mineralogist, published by the Mineralogical Society of America.
The published version is subject to change. Cite as Authors (Year) Title. American Mineralogist, in press.
DOI: https://doi.org/10.2138/am-2022-8415. http://www.minsocam.org/

surface (021)+As cluster				ΔC_L		
Surface	**element**	**CN**	**NN**	**min**	**max**	**mean**
1	As	2	S, Fe	0.01	0.01	0.01
1a	S	2	S(As), Fe	-0.12	-0.21	-0.16
1	As	2	As, Fe	-0.03	-0.03	-0.03
1	As	2	S, Fe	0.23	0.23	0.23
2a	S	4	S(As), 3Fe	0.03	-0.15	-0.06
2a	S	3	As, 2Fe	-0.19	-0.19	-0.19
2a	S	3	As, S, Fe	-0.01	-0.01	-0.01
2	As	3	As, 2Fe	0.06	0.06	0.06
2	As	1	S	0.29	0.29	0.29
2	As	3	S, 2Fe	0.20	0.20	0.20
2	As	4	2S, 2Fe	0.21	0.21	0.21
2	As	3	S, 2Fe	0.13	0.13	0.13
2	As	3	S, 2Fe	0.18	0.18	0.18
2c	S	4	S(As), 3Fe	0.00	-0.11	-0.03
3b	S	4	S(As), 3Fe	0.04	-0.11	-0.01
3b	S	3	3Fe	-0.01	-0.01	-0.01
3	As	3	S, 2Fe	0.21	0.21	0.21
3	As	4	4S	0.42	0.42	0.42
3	As	0	-	0.20	0.20	0.20
3	As	4	As, S,2Fe	0.12	0.12	0.12

Table 3(f): Löwdin atomic charge difference for (021) with As cluster. For S and As, ΔC_L is the charge difference with respect to bulk arsenian pyrite and bulk arsenopyrite respectively. CN and NN are coordination number and nearest neighbours respectively.

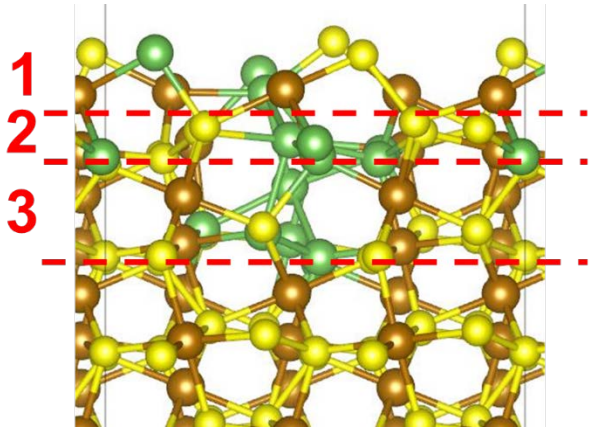

Figure 4(f): Schematic of (021) surface with an As cluster.

This is the peer-reviewed, final accepted version for American Mineralogist, published by the Mineralogical Society of America.
The published version is subject to change. Cite as Authors (Year) Title. American Mineralogist, in press.
DOI: https://doi.org/10.2138/am-2022-8415. http://www.minsocam.org/

surface (110)				ΔC_L		
Surface	**element**	**CN**	**NN**	**min**	**max**	**mean**
1a	S	2	S, Fe	-0.18	-0.18	-0.18
1c	S	3	S, 2Fe	-0.11	-0.13	-0.12
1d	S	4	S, 3Fe	0.07	-0.04	0.02
2b	S	4	S, 3Fe	0.04	0.03	0.04
2c	S	4	S, 3Fe	0.00	-0.01	0.00
3b	S	4	S, 3Fe	-0.02	-0.03	-0.03

Table 3(g): Löwdin atomic charge difference for (110) superficial layers. ΔC_L is the charge difference with respect to bulk arsenian pyrite. CN and NN are coordination number and nearest neighbours respectively.

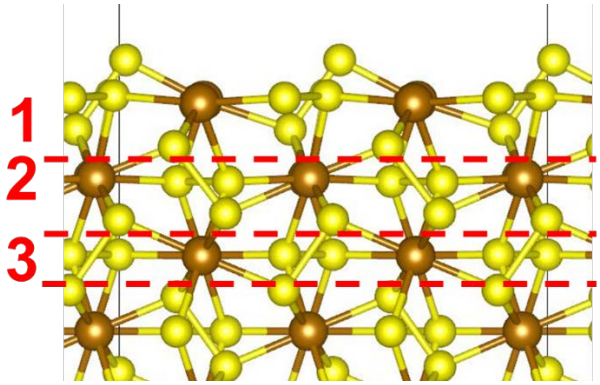

Figure 4(g): Schematic of (110) surface.

This is the peer-reviewed, final accepted version for American Mineralogist, published by the Mineralogical Society of America.
The published version is subject to change. Cite as Authors (Year) Title. American Mineralogist, in press.
DOI: https://doi.org/10.2138/am-2022-8415. http://www.minsocam.org/

surface (110)+3×As				ΔC_L		
Surface	**element**	**CN**	**NN**	**min**	**max**	**mean**
1	As	3	S, 2Fe	0.14	0.14	0.14
1a	S	2	S, Fe	-0.22	-0.29	-0.25
1b	S	3	S, 2Fe	-0.13	-0.20	-0.16
1	As	3	S, 2Fe	0.02	0.02	0.02
1	As	4	2S, 2Fe	0.03	0.03	0.03
1d	S	4	S, 3Fe	0.13	-0.14	0.01
2b	S	4	S, 3Fe	0.05	0.00	0.03
3a	S	4	S, 3Fe	0.01	-0.01	0.00

Table 3(h): Löwdin atomic charge difference for (110)+3×As superficial layers. For S and As, ΔC_L is the charge difference with respect to bulk arsenian pyrite and bulk arsenopyrite respectively. CN and NN are coordination number and nearest neighbours respectively.

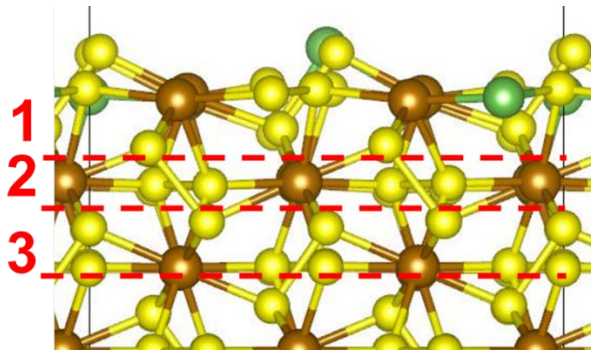

Figure 4(h): Schematic of (110) surface with 3x As atoms.

surface (111)				ΔC_L		
Surface	**element**	**CN**	**NN**	**min**	**max**	**mean**
1a	S	3	3Fe	-0.22	-0.29	-0.24
2b	S	4	S, 3Fe	0.01	-0.06	-0.03

Table 3(i): Löwdin atomic charge difference for (111) superficial layers. ΔC_L is the charge difference with respect to bulk arsenian pyrite. CN and NN are coordination number and nearest neighbours respectively.

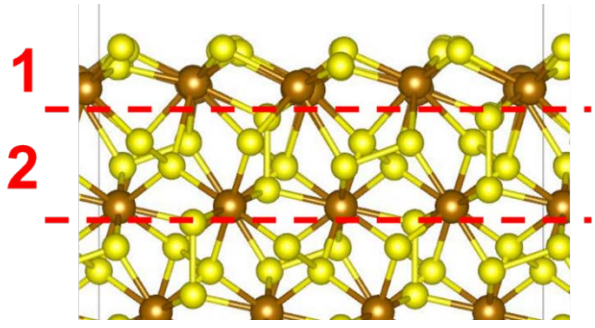

Figure 4(i): Schematic of (111) surface.

This is the peer-reviewed, final accepted version for American Mineralogist, published by the Mineralogical Society of America.
The published version is subject to change. Cite as Authors (Year) Title. American Mineralogist, in press.
DOI: https://doi.org/10.2138/am-2022-8415. http://www.minsocam.org/

surface (111)+3×As				ΔC_L		
Surface	**element**	**CN**	**NN**	**min**	**max**	**mean**
1	As	3	2S, Fe	0.14	0.14	0.14
1a	S	2	S, Fe	-0.08	-0.16	-0.13
1b	S	3	S(As), 2Fe	-0.11	-0.23	-0.16
1b	S	2	2Fe	-0.24	-0.24	-0.24
1	As	3	S, 2Fe	0.02	0.01	0.02
1d	S	4	S, 3Fe	0.11	-0.14	0.01
2a	S	4	S, 3Fe	0.05	0.02	0.04
2c	S	4	S, 3Fe	0.01	0.00	0.01

Table 3(j): Löwdin atomic charge difference for (111)+3×As superficial layers. For S and As, ΔC_L is the charge difference with respect to bulk arsenian pyrite and bulk arsenopyrite respectively. CN and NN are coordination number and nearest neighbours respectively.

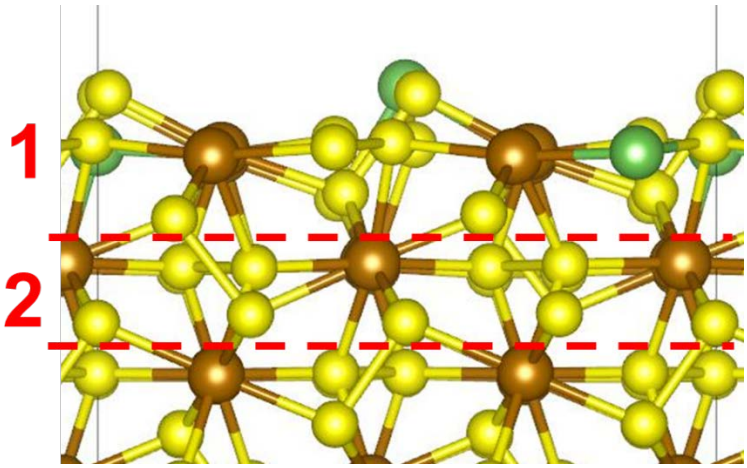

Figure 4(j): Schematic of (111) surface with 2x As atoms.

References

Alfonso, D.R. (2010) Computational Investigation of FeS2 Surfaces and Prediction of Effects of Sulfur Environment on Stabilities. The Journal of Physical Chemistry C, 114(19), 8971-8980.

Arehart, G.B., Chryssoulis, S.L., and Kesler, S.E. (1993) GOLD AND ARSENIC IN IRON SULFIDES FROM SEDIMENT-HOSTED DISSEMINATED GOLD DEPOSITS - IMPLICATIONS FOR DEPOSITIONAL PROCESSES. Economic Geology and the Bulletin of the Society of Economic Geologists, 88(1), 171-185.

Blanchard, M., Alfredsson, M., Brodholt, J., Wright, K., and Catlow, C.R.A. (2007a) Arsenic incorporation into FeS2 pyrite and its influence on dissolution: A DFT study. Geochimica et Cosmochimica Acta, 71(3), 624-630.

Blanchard, M., Wright, K., Gale, J.D., and Catlow, C.R.A. (2007b) Adsorption of As(OH)3 on the (001) Surface of FeS2 Pyrite: A Quantum-mechanical DFT Study. The Journal of Physical Chemistry C, 111(30), 11390-11396.

Bunz, J., Brink, T., Tsuchiya, K., Meng, F.Q., Wilde, G., and Albe, K. (2014) Low Temperature Heat Capacity of a Severely Deformed Metallic Glass. Physical Review Letters, 112(13).

Chen, J.-H., Li, Y.-Q., Zhong, S.-P., and Jin-Guo. (2013) DFT simulation of the occurrences and correlation of gold and arsenic in pyrite. American Mineralogist, 98(10), 1765-1771.

Cook, N.J., and Chryssoulis, S.L. (1990) CONCENTRATIONS OF INVISIBLE GOLD IN THE COMMON SULFIDES. Canadian Mineralogist, 28, 1-16.

Deditius, A.P., Utsunomiya, S., Renock, D., Ewing, R.C., Ramana, C.V., Becker, U., and Kesler, S.E. (2008) A proposed new type of arsenian pyrite: Composition, nanostructure and geological significance. Geochimica et Cosmochimica Acta, 72(12), 2919-2933.

Dos Santos, E.C., Lourenço, M.P., Pettersson, L.G.M., and Duarte, H.A. (2017) Stability, Structure, and Electronic Properties of the Pyrite/Arsenopyrite Solid–Solid Interface–A DFT Study. The Journal of Physical Chemistry C, 121(14), 8042-8051.

Dronskowski, R. (2005) Computational Chemistry of Solid State Materials. Wiley, Weinheim.

Dudarev, S.L., Botton, G.A., Savrasov, S.Y., Humphreys, C.J., and Sutton, A.P. (1998) Electron-energy-loss spectra and the structural stability of nickel oxide: An LSDA+U study. Physical Review B, 57(3), 1505-1509.

Ennaoui, A., Fiechter, S., Pettenkofer, C., Alonso-Vante, N., Büker, K., Bronold, M., Höpfner, C., and Tributsch, H. (1993) Iron disulfide for solar energy conversion. Solar Energy Materials and Solar Cells, 29(4), 289-370.

Ertural, C., Steinberg, S., and Dronskowski, R. (2019) Development of a robust tool to extract Mulliken and Löwdin charges from plane waves and its application to solid-state materials. RSC Advances, 9(51), 29821-29830.

Harmer, S.L., and Nesbitt, H.W. (2004) Stabilization of pyrite (FeS2), marcasite (FeS2), arsenopyrite (FeAsS) and loellingite (FeAs2) surfaces by polymerization and auto-redox reactions. Surface Science, 564(1), 38-52.

Hu Yuehua, Sun Wei, and Dianzuo, W. (2009) Electrochemistry of Flotation of Sulphide Minerals. Springer, Springer Berlin.

Jones, R.A., Koval, S.F., and Nesbitt, H.W. (2003) Surface alteration of arsenopyrite (FeAsS) by Thiobacillus ferrooxidans. Geochimica et Cosmochimica Acta, 67(5), 955-965.

Kresse, G., and Furthmuller, J. (1996) Efficient iterative schemes for ab initio total-energy calculations using a plane-wave basis set. Physical Review B, 54(16), 11169-11186.

Kresse, G., and Joubert, D. (1999) From ultrasoft pseudopotentials to the projector augmented-wave method. Physical Review B, 59(3), 1758-1775.

Krishnamoorthy, A., Herbert, F.W., Yip, S., Van Vliet, K.J., and Yildiz, B. (2012) Electronic states of intrinsic surface and bulk vacancies in FeS2. Journal of Physics: Condensed Matter, 25(4), 045004.

Le Pape, P., Blanchard, M., Brest, J., Boulliard, J.-C., Ikogou, M., Stetten, L., Wang, S., Landrot, G., and Morin, G. (2017) Arsenic Incorporation in Pyrite at Ambient Temperature at Both Tetrahedral S–I and Octahedral FeII Sites: Evidence from EXAFS–DFT Analysis. Environmental Science & Technology, 51(1), 150-158.

Liang, J.-l., Sun, W.-d., Li, Y.-l., Zhu, S.-y., Li, H., Liu, Y.-l., and Zhai, W. (2013) An XPS study on the valence states of arsenic in arsenian pyrite: Implications for Au deposition mechanism of the Yang-shan Carlin-type gold deposit, western Qinling belt. Journal of Asian Earth Sciences, 62, 363-372.

Mahjoub, R., Ferry, M., and Stanford, N. (2019) Local topology and its effects on grain boundary and solute segregation in HCP magnesium. Materialia, 6, 100258.

Momma, K., and Izumi, F. (2011) Vesta 3 for three-dimensional visualization of crystal, volumetric and morphology data. Journal of Applied Crystallography, 44, 24.

Murphy, R., and Strongin, D.R. (2009) Surface reactivity of pyrite and related sulfides. Surface Science Reports, 64(1), 1-45.

Nesbitt, H.W., Muir, I.J., and Prarr, A.R. (1995) Oxidation of arsenopyrite by air and air-saturated, distilled water, and implications for mechanism of oxidation. Geochimica et Cosmochimica Acta, 59(9), 1773-1786.

Nesbitt, H.W., Uhlig, I., and Szargan, R. (2002) Surface reconstruction and As-polymerization at fractured loellingite (FeAs2) surfaces. American Mineralogist, 87(7), 1000-1004.

Palenik, C.S., Utsunomiya, S., Reich, M., Kesler, S.E., Wang, L.M., and Ewing, R.C. (2004) "Invisible" gold revealed: Direct imaging of gold nanoparticles in a Carlin-type deposit. American Mineralogist, 89(10), 1359-1366.

590 Perdew, J.P., Burke, K., and Ernzerhof, M. (1996) Generalized gradient approximation made simple.
591 Physical Review Letters, 77(18), 3865-3868.
592 Persson, K., Ceder, G., and Morgan, D. (2006) Spin transitions in the Fe-Mn-S system. Physical
593 Review B, 73(11), 115201.
594 Pierre, L.P., Marc, B., Amélie, J., Jean-Pascal, R., Manoj, D., Guillaume, M., and Delphine, C. (2018)
595 Local environment of arsenic in sulfide minerals: insights from high-resolution X-ray
596 spectroscopies, and first-principles calculations at the As K-edge. Journal of Analytical
597 Atomic Spectrometry, 33(12), 2070-2082.
598 Reich, M., and Becker, U. (2006) First-principles calculations of the thermodynamic mixing
599 properties of arsenic incorporation into pyrite and marcasite. Chemical Geology, 225(3), 278-
600 290.
601 Reich, M., Kesler, S.E., Utsunomiya, S., Palenik, C.S., Chryssoulis, S.L., and Ewing, R.C. (2005)
602 Solubility of gold in arsenian pyrite. Geochimica et Cosmochimica Acta, 69(11), 2781-2796.
603 Richter, B., Kuhlenbeck, H., Freund, H.J., and Bagus, P.S. (2004) Cluster Core-Level Binding-Energy
604 Shifts: The Role of Lattice Strain. Physical Review Letters, 93(2), 026805.
605 Rohrbach, A., Hafner, J., and Kresse, G. (2003) Electronic correlation effects in transition-metal
606 sulfides. Journal of Physics: Condensed Matter, 15(6), 979-996.
607 Savage, K.S., Tingle, T.N., O'Day, P.A., Waychunas, G.A., and Bird, D.K. (2000) Arsenic speciation
608 in pyrite and secondary weathering phases, Mother Lode Gold District, Tuolumne County,
609 California. Applied Geochemistry, 15(8), 1219-1244.
610 Schaufuß, A.G., Nesbitt, H.W., Kartio, I., Laajalehto, K., Bancroft, G.M., and Szargan, R. (1998)
611 Reactivity of surface chemical states on fractured pyrite. Surface Science, 411(3), 321-328.
612 Schaufuss, A.G., Nesbitt, H.W., Scaini, M.J., Hoechst, H., Scaini, M.J., and Szargan, R. (2000)
613 Reactivity of surface sites on fractured arsenopyrite (FeAsS) toward oxygen. American
614 Mineralogist, 85(11-12), 1754-1766.
615 Simon, G., Huang, H., Penner-Hahn, J.E., Kesler, S.E., and Kao, L.-S. (1999) Oxidation state of gold
616 and arsenic in gold-bearing arsenian pyrite. American Mineralogist, 84(7-8), 1071-1079.
617 Stepanov, A.S., Large, R.R., Kiseeva, E.S., Danyushevsky, L.V., Goemann, K., Meffre, S., Zhukova,
618 I., and Belousov, I.A. (2021) Phase relations of arsenian pyrite and arsenopyrite. Ore Geology
619 Reviews, 136, 104285.
620 Sun, R., Chan, M.K.Y., and Ceder, G. (2011) First-principles electronic structure and relative stability
621 of pyrite and marcasite: Implications for photovoltaic performance. Physical Review B,
622 83(23), 235311.
623 Sung, Y.H., Brugger, J., Ciobanu, C.L., Pring, A., Skinner, W., and Nugus, M. (2009) Invisible gold
624 in arsenian pyrite and arsenopyrite from a multistage Archaean gold deposit: Sunrise Dam,
625 Eastern Goldfields Province, Western Australia. Mineralium Deposita, 44(7), 765.

626 von Oertzen, G.U., Skinner, W.M., and Nesbitt, H.W. (2005) Ab initio and x-ray photoemission
627 spectroscopy study of the bulk and surface electronic structure of pyrite (100) with
628 implications for reactivity. Physical Review B, 72(23), 235427.
629 Wells, J.D., and Mullens, T.E. (1973) Gold-Bearing Arsenian Pyrite Determined by Microprobe
630 Analysis, Cortez and Carlin Gold mines, Nevada. Economic Geology, 68(2), 187-201.
631 Zhang, Y.N., Hu, J., Law, M., and Wu, R.Q. (2012) Effect of surface stoichiometry on the band gap
632 of the pyrite (100) surface. Physical Review B, 85(8), 085314.

633